JGR Atmospheres

Key Points:

- A 3D sub-grid terrain solar radiative effect scheme has been applied in the Weather Research and Forecasting model and its impact on weather forecast has been studied
- The 3-dimensional sub-grid terrain solar radiative effect reduces the overestimation of surface solar radiation, leading to the thermal low over the Tibetan Plateau weakened
- The weakened thermal low together with the more stable atmosphere reduces the overestimation of precipitation forecast over Tibetan Plateau

Correspondence to:
A. Huang and K. Zhu,
anhuang@nju.edu.cn;
zhukf@cma.gov.cn

Author Contributions:
Conceptualization: Anning Huang, Kefeng Zhu
Data curation: Shuxin Cai, Yang Wu
Formal analysis: Shuxin Cai
Investigation: Shuxin Cai, Weidong Guo
Methodology: Shuxin Cai, Anning Huang, Kefeng Zhu, Chunlei Gu
Project Administration: Anning Huang, Weidong Guo
Resources: Shuxin Cai
Software: Shuxin Cai, Yang Wu, Chunlei Gu
Supervision: Anning Huang, Kefeng Zhu
Validation: Shuxin Cai, Yang Wu
Visualization: Shuxin Cai, Anning Huang
Writing – original draft: Shuxin Cai, Anning Huang, Kefeng Zhu, Weidong Guo, Chunlei Gu

The Forecast Skill of the Summer Precipitation Over Tibetan Plateau Improved by the Adoption of a 3D Sub-Grid Terrain Solar Radiative Effect Scheme in a Convection-Permitting Model

Shuxin Cai[1,2], Anning Huang[1] , Kefeng Zhu[2] , Weidong Guo[1] , Yang Wu[2], and Chunlei Gu[1]

[1]School of Atmospheric Sciences, Nanjing University, Nanjing, China, [2]CMA Key Laboratory of Transportation Meteorology, Nanjing Joint Institute for Atmospheric Sciences, Nanjing, China

Abstract We have successfully incorporated a 3-dimensional sub-grid terrain solar radiative effect (3D STSRE) parameterization scheme into a convection-permitting Weather Research and Forecasting model (WRF_CPM) in this study. Impacts of 3D STSRE scheme on the ability of WRF_CPM in forecasting the precipitation in summer over the Tibetan Plateau (TP) and nearby regions with complex terrain have been systematically addressed by conducting experiments without and with the 3D STSRE scheme. Results show that the application of 3D STSRE scheme can obviously mitigate the overestimation of surface solar radiation (SSR) and rainfall over TP and nearby regions, especially over the areas with much more rugged terrain (i.e., southern TP) in the WRF_CPM without 3D STSRE scheme. Further mechanism analyses indicate that the decreased surface heating induced by the reduction of SSR reduces the intensity of the thermal-low pressure over the TP, which leads to the diminished strength of southwesterly winds and thereafter the weaker convergence of moisture flux over the southern TP. Moreover, the weakened surface thermal forcing makes the local atmosphere more stable, suppressing the vertical water vapor transport and local convection. These effects greatly alleviate the overestimation of precipitation over the southern TP produced by the WRF_CPM without the 3D STSRE scheme.

Plain Language Summary The sub-grid terrain solar radiative effect (STSRE) is crucial to land-air interaction, especially over the regions with complicated terrain, such as the Tibetan Plateau (TP). While the plane-parallel radiative scheme which neglects the STSRE on the surface solar radiation (SSR) is used in most current weather models. Inaccurate depiction of SSR would cause large biases in the surface temperature and precipitation forecast. In this study, a newly developed 3-dimensional (3D) STSRE scheme with solid physical processes and accurate sub-grid terrain features is introduced into a convection-permitting Weather Research and Forecasting (WRF_CPM) model. Results indicate that the adoption of 3D STSRE scheme can reduce the overestimation of the SSR and precipitation over the TP. Findings of this work emphasize the importance of considering the STSRE in high-resolution weather models and provide an effective way to improve the short-range precipitation forecast over regions with complex terrain.

1. Introduction

The Tibetan Plateau (TP) covers a vast area and has a mean elevation of 4,000 m, which is regarded as the "third pole." It is crucial to global climate simulation and weather forecasting (Y. C. Gao & Liu, 2013; Qiu, 2008; C. Zhang et al., 2017). Inaccurate parameterizations of the thermal and dynamical effects of the inhomogeneous topography lead to large forecast or simulation biases over the TP (Lin et al., 2018; R. Yu et al., 2014).

In recent decades, adopting parameterization schemes and increasing the model horizontal resolution substantially improved the precipitation forecast on the TP (Y. Gao et al., 2017; Kan et al., 2015; Y. Wang et al., 2020; Xu et al., 2018). However, the precipitation simulations over TP still display obvious wet biases (P. Li et al., 2021; X. Wang et al., 2018). The wet biases are attributed to the unreasonable representations of thermo-dynamical processes caused by the sub-grid terrain (Y. Gao et al., 2017; Jiménez & Dudhia, 2013; Lee et al., 2015; Wu & Chen, 1985; Zhou et al., 2019). Dynamical parameterizations including the gravity wave drag and turbulent orographic form drag have been developed to improve sub-grid orographic drag processes (Kim & Doyle, 2005; McFarlane, 1987; Wooding et al., 1973). Due to the better description of the unresolved sub-grid orographic

drag, the wind fields and background circulation are more realistically simulated (Choi et al., 2017; Lindvall et al., 2013). Inaccurate simulation of the surface thermal condition is another important factor for the large wet biases over the TP (Helbig & Löwe, 2012; Manners et al., 2012; Y. Zhang et al., 2006). Most numerical models adopt the plane-parallel radiative transfer schemes, where the topography is supposed flat without considering the influences of sub-grid orographic factors (i.e., terrain slope, orientation, sky visibility and reflection of nearby terrains) on surface solar radiation (SSR). Thus, the SSR calculated by plane-parallel radiative schemes mainly varies with latitude and cannot reflect the inhomogeneous distribution of SSR over rugged regions (Gu et al., 2022; Hao et al., 2022; Liou et al., 2013; Müller & Scherer, 2005).

Several sub-grid terrain solar radiative effect (STSRE) parameterizations have been developed and implemented into climate and weather models. Y. Zhang et al. (2006) used the 2-dimensional (2D) STSRE scheme that includes the effects of terrain slope and aspect to explicitly correct the original SSR in a regional climate model. The modified model reproduced more realistic temperature on the TP and mitigated the overestimation of summer rainfall over southern China. Gu et al. (2020) proposed a 2D STSRE scheme by averaging the sub-grid orographic factors onto the model grid before the model integration. Their results showed that the adoption of the 2D STSRE scheme in the Regional Climate Model (RegCM) reduced the net SSR and led to a weaker west (Chinese mainland)east (tropical oceans) thermal contrast and thereafter a weakened East Asian summer monsoon, which resulted in less moisture transport and improved precipitation simulation over most areas of China.

However, the 2D STSRE scheme only includes the terrain slope and aspect of itself (Kondrat'yev, 1965). Large overestimation of the SSR are found during sunrise or sunset due to the ignorance of the reflecting and shading effects from the nearby terrains (Arthur et al., 2018; Y. Zhang et al., 2006). Recently, a 3D Monte Carlo ray tracing method was developed by Chen et al. (2006) and simplified by Lee et al. (2011). Compared with the 2D STSRE scheme, the 3D Monte Carlo program considers both influences of self-shadowing and multiple reflection from surrounding terrains. This 3D Monte Carlo scheme has been incorporated in the Community Climate System Model and alleviated the underestimation of surface temperature by 13% through reducing the biases of upward shortwave fluxes on the southern and central of TP (Lee et al., 2019). Gu et al. (2012) also applied the 3D Monte Carlo program into the WRF model and conducted a case simulation in March. They found that deviations of SSR were up to ± 50 W·m^{-2}, which lead to the increasing of surface temperature, snowmelt and soil moisture on sunny slope. The cloud water path decreased due to the changes in surface heat and energy fluxes.

Although the 3D Monte Carlo method considers the combined effects of the self and nearby terrains on SSR, this scheme was only tested in the TP region and Rocky Mountains (Gu et al., 2012; Liou et al., 2007). The regression coefficients of the parameterized equations were merely tested at specific regions with several surface albedo and solar elevation angles (Huang et al., 2022).

Beside the deficiencies in STSRE modeling, studies mostly focused on the climatic impacts of STSRE (Gu et al., 2012, 2020, 2022; Hauge & Hole, 2003; Liou et al., 2013). The STSRE has direct impact on the surface temperature forecast and thus can directly influence the weather, such as the precipitation diurnal variation (Colette et al., 2003; Huang & Qian, 2008; Müller & Scherer, 2005). Though the influence of sub-grid terrain on SSR intensifies with the increasing horizontal resolution (Hao et al., 2021; Huang et al., 2022), the performance of STSRE in high resolution weather forecasting has not been systematically evaluated. For these reasons, a 3D STSRE scheme with more accurate sub-grid terrain features and easier for coupling is in need, and the impacts of 3D STSRE on the capability of the WRF model at a convection-permitting scale (WRF_CPM) deserves further study.

Recently, we have developed a 3D STSRE scheme to involve the sub-grid topographic inhomogeneity, shadowing and reflecting effects of surrounding terrains on each sub-grid according to the mountainous radiation theory (Huang et al., 2022). Based on the elevation data with high resolution, we calculate the sub-grid topographic factors and aggregate them onto the model grid before the model integration. This can ensure the precision of the sub-grid topographic traits without adding computing resources. X. Zhang et al. (2022) has applied the 3D STSRE scheme into the Common Land Model (CoLM) and significantly improved the simulations of soil temperature and moisture. In this work, the 3D STSRE scheme is introduced in the WRF_CPM model to enhance the representation of surface radiation processes over TP with steep mountainous regions. Impacts of 3D STSRE scheme on the precipitation forecast over TP and nearby areas in summer and underlying mechanisms have been systematically examined.

2. Data, Model and Methodology

2.1. Observation Data

The datasets for model evaluation are listed as follows.

1. The 5-km East Asia-Pacific surface longwave/shortwave downward radiation based on the Himawari-8 obtained from National Tibetan Plateau Data Center (Letu et al., 2022). The influences of cloud, topography and high aerosol loadings on the SSR are fully considered in this data set. Evaluation using ground observations shows that this data set has higher accuracy compared with other reanalysis or satellite-derived datasets over the entire East Asia–Pacific (Letu et al., 2022).
2. The $0.05° × 0.05°$, hourly precipitation is derived from the merged rainfall product which combines more than 30,000 rain-gauge observations with the rainfall estimation of the Climate Prediction Center's morphing rainfall estimates (CMORPH; Joyce et al., 2004). The data set owns the merits of the satellite measured rainfall and rain gauge record. The systematic errors and RMSE of this gauge-satellite merged data set are much smaller when compared to the original CMORPH data (Shen et al., 2014). Previous validations showed that this merged precipitation data is reliable for annual and summer rainfall study over China (Shen et al., 2010; B. Yu et al., 2020; Zhu et al., 2021). Several recent studies have used this product to conduct model evaluations and mechanism analysis of precipitation over the TP (Cai et al., 2021; P. Li et al., 2021; Y. Wu et al., 2018).

2.2. The WRF_CPM and 3D STSRE Scheme

The official Advanced Research WRF Version 4.2 (WRF-ARW V4.2; Skamarock et al., 2019) at a convection-permitting scale (~4 km; WRF_CPM) is used in this study. Though the WRF_CPM model proved well to resolve the complicated terrain (Lin et al., 2018), the current radiation scheme used in WRF_CPM model is the plane-parallel scheme, which cannot well reflect the STSRE. The inconsistency between the high resolution and unreasonable depiction of the STSRE would cause large errors. Thus, the plane-parallel scheme in WRF_CPM model is not suitable for steep mountainous regions such as the TP. According to Huang et al. (2022), we couple the 3D STSRE scheme within the WRF_CPM model. The core of the coupling procedure is to correct the original SSR components using the STSRE parameters based on Equations 1–3. Here, we briefly summarize the 3D STSRE scheme. Detailed definitions and calculations can be referred to Huang et al. (2022).

First, the terrain slope α_k (0 ~ 90°), aspect β_k (0 ~ 360°) and sky view factor SVF_k (0 ~ 1) of each sub-grid k are derived from the Shuttle Radar Topography Mission (SRTM) global elevation data set with the resolution of 3 arc seconds (~90 m) (Jarvis et al., 2008) for the subsequent calculation of STSRE parameters.

Second, the sub-grid (~90 m resolution) terrain parameters related to the 3D STSRE scheme are upscaled to the model grids with the horizontal resolution of ~4 km based on the method of Huang et al. (2022) before the model integration. The U_g, V_g, W_g, DIF_g and REF_g (Equations 1–5) at each model grid g are calculated based on the mountain radiation theory (Dozier & Frew, 1990; Huang et al., 2022; J. Li & Luo, 2015). These parameters are only associated with the 3D sub-grid topographic features (terrain slope α, aspect β, and sky view factor SVF) and are time-invariable. The U_g is linked with area of the rugged surface, V_g and W_g are related to the solar incident angle on the rugged surface. The DIF_g and REF_g are relevant to the diffuse and reflected radiation respectively. Other two parameters including the shading factor SF_g and parameter DIR_g are achieved by the combination of time-invariant STSRE parameters and the time-variant solar azimuth angle θ_g and the solar zenith angle Z_g at every model time step (Equations 6 and 7). C_{ad} is the adjustment factor and is 0.071 under the grid spacing (dx) of 4 km in this paper (Equation 8). The operator $<>_{k \to g}$ represents averaging the values of all the sub grids within the model grid g. Huang et al. (2022) have indicated that results from the offline calculation of 3D STSRE parameterization is equivalent to the explicit calculation of the SSR components on each sub-grid point.

$$U_g = < \sec \alpha_k >_{k \to g} = \frac{1}{n} \sum_{k=1}^{k=n} \sec \alpha_k \tag{1}$$

$$V_g = < \tan \alpha_k \cos \beta_k >_{k \to g} = \frac{1}{n} \sum_{k=1}^{k=n} \tan \alpha_k \cos \beta_k \tag{2}$$

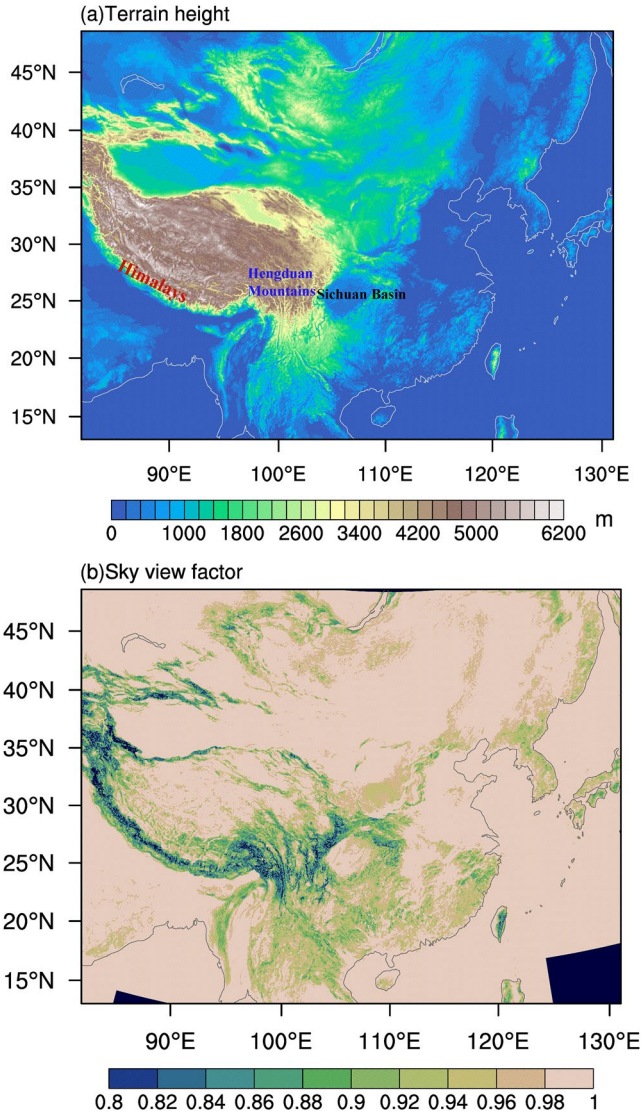$$W_g = < \tan \alpha_k \sin \beta_k >_{k \to g} = \frac{1}{n} \sum_{k=1}^{k=n} \tan \alpha_k \sin \beta_k \tag{3}$$

Figure 1. The spatial distributions of topography (a) and sky view factor (b) at the horizontal resolution of ~4 km.

$$DIF_g = < \frac{\sec \alpha_k SVF_k}{2}(1 + \cos \alpha_k) >_{k \to g}$$
$$= \frac{1}{n} \sum_{k=1}^{k=n} \frac{\sec \alpha_k SVF_k}{2}(1 + \cos \alpha_k) \qquad (4)$$

$$REF_g = < \left(\frac{1 + \cos \alpha_k}{2} - SVF_k \right) \sec \alpha_k >_{k \to g}$$
$$= \frac{1}{n} \sum_{k=1}^{k=n} \left(\frac{1 + \cos \alpha_k}{2} - SVF_k \right) \sec \alpha_k \qquad (5)$$

$$SF_g = 1 - C_{ad}(1 - < SF_k >_{k \to g}) \qquad (6)$$

$$DIR_g = \cos Z_g + V_g \sin Z_g \cos \theta_g + W_g \sin Z_g \sin \theta_g \qquad (7)$$

$$C_{ad} = 0.1849 dx^{-1.443} + 0.04561 \qquad (8)$$

Third, the original downward SSR components in the plane-parallel scheme is corrected using the STSRE parameters based on Equations 9–11 during the model integration. Here, the $S_{dir,ter_g\downarrow}$ $(S_{dir_g\downarrow})$ and $S_{dif,ter_g\downarrow}$ $(S_{dif_g\downarrow})$ on the left (right) hand of Equations 9–10 are the corrected (original) direct and diffuse solar radiation fluxes on the rugged (plane) surface. The $S_{ref,ter_g\downarrow}$ is the reflected radiation from surrounding terrains on rugged surface. The S_0 and a_g are the solar constant and surface albedo.

$$S_{dir,ter_g\downarrow} = \max \left(SF_g \cdot DIR_g \frac{S_{dir_g\downarrow}}{\cos Z_g} / U_g, 0.0 \right) \qquad (9)$$

$$S_{dif,ter_g\downarrow} = \begin{cases} S_{dif_g\downarrow} \left[\frac{S_{dir,ter_g\downarrow}}{S_0} + DIF_g \left(1 - \frac{S_{dir_g\downarrow}}{S_0} \right) / U_g \right], \text{if } DIR_g > 0 \\ S_{dif_g\downarrow} \left[DIF_g \left(1 - \frac{S_{dir_g\downarrow}}{S_0} \right) / U_g \right], \quad \text{otherwise} \end{cases} \qquad (10)$$

$$S_{ref,ter_g\downarrow} = \left(S_{dir_g\downarrow} + S_{dif_g\downarrow} \right) a_g REF_g / U_g \qquad (11)$$

Finally, based on the energy conservation theory, the differences of downward SSR components between the plane parallel scheme and the 3D STSRE scheme should be returned to the atmosphere via the upward solar radiation fluxes. Therefore, the upward SSR components are adjusted by the equivalent albedo at the bottom level of atmosphere (Huang et al., 2022):

$$S_{dir,ter_g\uparrow} = S_{dir,ter_g\downarrow} \cdot \left(a_g + \frac{S_{dir_g\downarrow} - S_{dir,ter_g\downarrow}}{S_{dir,ter_g\downarrow}} \right) \qquad (12)$$

$$S_{dif,ter_g\uparrow} = \left(S_{dif,ter_g\downarrow} + S_{ref,ter_g\downarrow} \right) \cdot \left(a_g + \frac{S_{dif_g\downarrow} - (S_{dif,ter_g\downarrow} + S_{ref,ter_g\downarrow})}{S_{dif,ter_g\downarrow} + S_{ref,ter_g\downarrow}} \right) \qquad (13)$$

where the $S_{dir,ter_g\uparrow}$ and $S_{dif,ter_g\uparrow}$ are the corrected upward direct and diffuse radiation components. Note that the reflected radiation flux $S_{ref,ter_g\downarrow}$ in the 3D STSRE scheme is added to the downward diffuse radiation flux $S_{dif,ter_g\downarrow}$ in Equation 13 since the reflected radiation fluxes from nearby terrains are not considered in the plane-parallel scheme (Arnold et al., 2006; Hock & Holmgren, 2005).

2.3. Methodology

2.3.1. Experiment Design

In this study, two experiments namely CTRL (without the 3D STSRE scheme) and STSRE (with the 3D STSRE scheme) are carried out to explore the influences of STSRE on the precipitation forecast. Here, we primarily focus on the TP and nearby regions with complex terrain.

Table 1
The Contingency Table

Forecast		Observed		
		Yes	No	Total
	Yes	Hits	False alarms	Forecast yes
	No	Misses	Correct negatives	Forecast no
	Total	Observed yes	Observed no	Total

The simulation domain covers the whole China with the horizontal resolution at 4 km (Figure 1a). It has 1,080 grids south-north and 1,408 grids east-west with the center at 105.5°E, 36.0°N, and 50 vertical levels. From Figure 1a, the terrain height ranges from 0 to 6200m over the model domain. Figure 1b shows the distribution of SVF which reflects topographic relief. Lower SVF denotes much more rugged terrains. Clearly, the SVF shows much smaller values along the northwestern, southern and eastern slopes of TP, where the terrain undulates violently (Figure 1b).

The main physical parameterization schemes are the CAM shortwave and longwave radiation schemes (Collins et al., 2004), the NOAH land surface model (Chen & Dudhia, 2001), the Yonsei University planetary boundary layer scheme (YSU; Hong et al., 2006) and the WRF Single-Moment 5-class microphysics (WSM5; Hong et al., 2004). Since the convection is mostly resolvable at 4 km grid resolution (Weisman et al., 1997; Zhu et al., 2018). Also, the cumulus parameterization scheme if not scale adaptive, will produce excessive rainfall at ~4 km grid (Prein et al., 2015). Thus, we switch off the cumulus parameterization scheme. The model is driven by the initial and lateral boundary conditions of the 3 hourly, 0.25° × 0.25° NCEP Global Forecast System real-time forecasts (NCEP, 2015). We conduct rolling forecast of 36 hr starting at 00:00 UTC on each day in June 2020 for each experiment. The first 12 hr is taken as the model spin-up time. The results of the last 24 hr for each forecast are used for analysis.

2.3.2. Validation Metrics and Analysis Method

The criterion of valid precipitation is over 0.1 mm·hr^{-1} at 1 hour in each day. We use equitable threat score (ETS) and frequency bias (FBIAS) for evaluation of the precipitation forecast. FBIAS is the ratio of the correctly predicted rain area (frequency) to the observed rainfall area (frequency), which ranges between zero to infinity and the best score is 1.0 (Equation 14). ETS stands for the accuracy of forecasting, it includes the influences of regions, climate and environment on precipitation forecast. The perfect score for ETS is 1.0 (Equations 15 and 16). First, we use 0.1 and 10 mm thresholds to evaluate the occurrence of rainfall based on the 12 hr accumulated rainfall of each day. Then, the forecasts are stratified into four categories shown in Table 1. Finally, we sum up the four kinds of results of each day and calculate the ETS and FBIAS scores according to Equations 14–16 (Ebert et al., 2003; Mesinger & Black, 1992; C. C. Wang, 2014). We use the Model Evaluation Tools (MET) package established by the Development Testbed Center to calculate FBIAS and ETS scores (Brown et al., 2009).

$$\text{FBIAS} = \frac{\text{hits} + \text{false alarms}}{\text{hits} + \text{misses}} \tag{14}$$

$$\text{ETS} = \frac{\text{hits} - \text{hits}_{\text{random}}}{\text{hits} + \text{misses} + \text{false alarms} - \text{hits}_{\text{random}}} \tag{15}$$

where

$$\text{hits}_{\text{random}} = \frac{(\text{hits} + \text{misses})(\text{hits} + \text{false alarms})}{\text{total}} \tag{16}$$

To better investigate the change of moisture transport on precipitation, we conduct a moisture budget analysis by following the previous studies (Chou & Lan, 2012; P. Li et al., 2020; Lin et al., 2014). The moisture budget equation at the p level coordinate is:

$$P = -\frac{1}{g}\int_{p_s}^{p_t} \frac{\partial q}{\partial t} dp - \frac{1}{g}\int_{p_s}^{p_t} \nabla_h \cdot \left(q\,\vec{V_h}\right) dp - \frac{1}{g}\int_{p_s}^{p_t} \frac{\partial \omega q}{\partial p} dp + E + \delta \tag{17}$$

where "P" on the left side of Equation 17 denotes the precipitation rate, "q" is the specific humidity. "$\frac{\partial q}{\partial t}$" indicates the changes of local moisture. "$-\nabla_h \cdot \left(q\,\vec{V_h}\right)$" is the convergence of horizontal moisture flux. "ω" is the vertical velocity at the p level coordinate and "$\frac{\partial \omega q}{\partial p}$" denotes the vertical transport of moisture flux. "$\int_{p_s}^{p_t} A$" indicates a vertical integration from the surface (p_s) to the top of the tropopause (p_t) and "g" represents the gravity acceleration. "E" represents the evaporation rate. The residual term "δ" includes the surface processes linking with topography and model bias (Ma & Zhou, 2015; Seager et al., 2010).
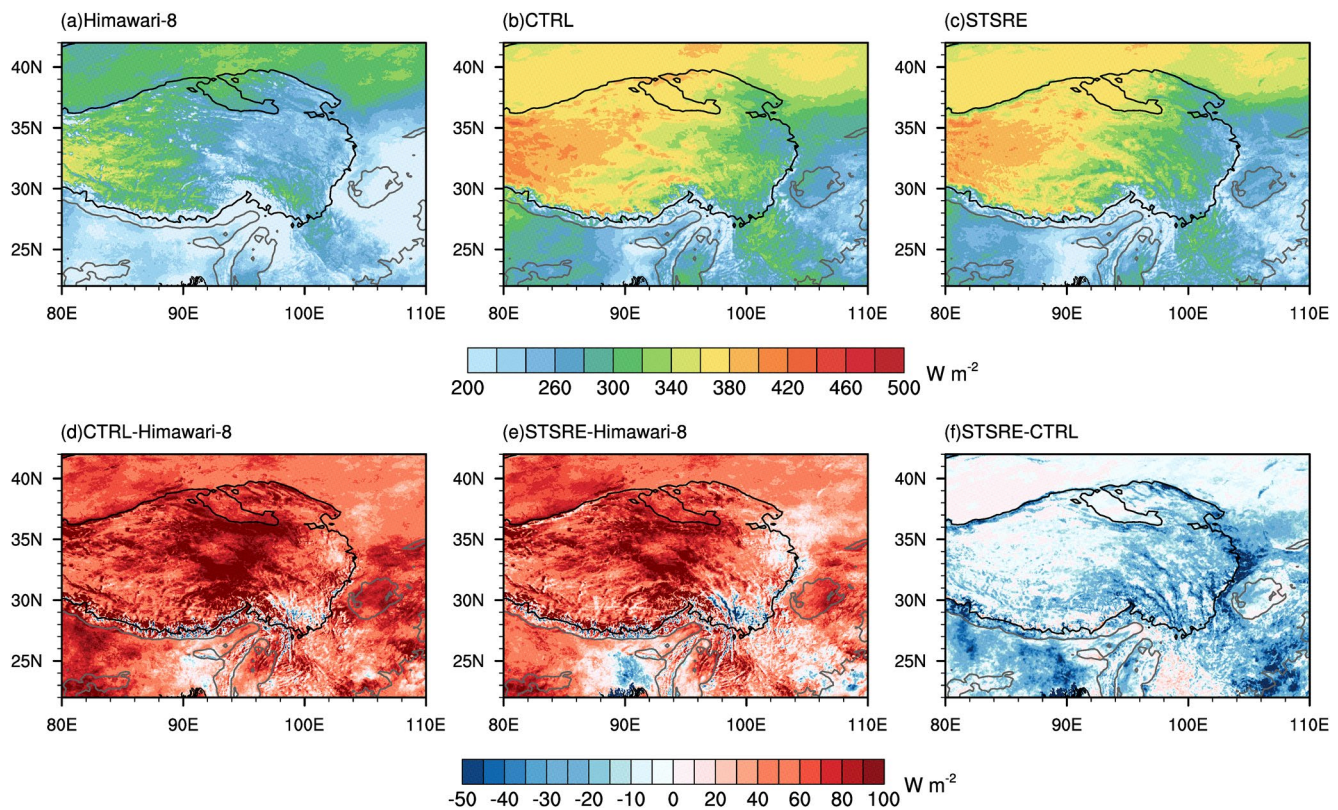
Figure 2. The spatial distributions of the mean surface solar radiation in June 2020 from the Himawari-8 (a), CTRL (b) and sub-grid terrain solar radiative effect (STSRE) experiments (c) with the differences between CTRL and Himawari-8 (d), between STSRE and Himawari-8 (e) and between STSRE and CTRL (f). The black (gray) lines denote the terrain height of 3,000 (500) m.

3. Results

3.1. Downward Surface Solar Radiation

The mean SSR in June 2020 derived from the Himawari-8 observation, forecasts from the CTRL and STSRE experiments and their differences are presented in Figure 2. The observed SSR increases from the southeastern to northwestern TP with relatively larger values over Hengduan Mountains, northern TP as well as relatively flat areas in the northwest of the domain (Figure 2a). Both CTRL and STSRE experiments can properly reproduce the distribution of SSR but overestimate the magnitude (Figures 2b and 2c). Compared to the Himawari-8 retrieved SSR, the CTRL experiment clearly overestimates the intensity of SSR, with the domain-averaged bias up to 64 W·m^{-2} (Figures 2b and 2d). As shown in Figure 2e, the implementation of the STSRE can obviously reduce the overestimated SSR by a reduction of ~50 W·m^{-2} along the Hengduan Mountains and Sichuan basin. The large decrease in SSR is mainly contributed by the shadowing effects from the surrounding terrains on direct solar radiation flux (not shown) over the steep regions.

The SSR is smaller (larger) when the target point is obstructed (unobstructed) by surrounding terrains with SVF approaching 0 (1). To investigate the impacts of 3D STSRE on the SSR under different openness of terrains, the mean diurnal variations of the SSR and RMSE between the Himawari-8 and two experiments averaged within each category of SVF are shown in Figure 3. According to the Himawari-8 observation, the diurnal cycle of SSR has a prominent peak at 14:00 Beijing time (BJT) during the afternoon. The peak value is ~790 W·m^{-2} under the condition of SVF greater than 0.99, yet the peak value is decreased to ~558 W·m^{-2} when the SVF is less than 0.8, suggesting the topographic shading effects on the SSR (Figures 3a and 3g). Both the CTRL and STSRE experiments well capture the diurnal patterns of the SSR under different categories of SVF but show a general overestimation. It is notable that the evident overestimation of SSR in the CTRL experiment is mitigated after implementing the 3D STSRE scheme, and such improvement is more obvious under smaller SVF conditions. When the SVF is smaller than 0.8, the CTRL experiment shows a maximal diurnal bias of ~303 W·m^{-2}
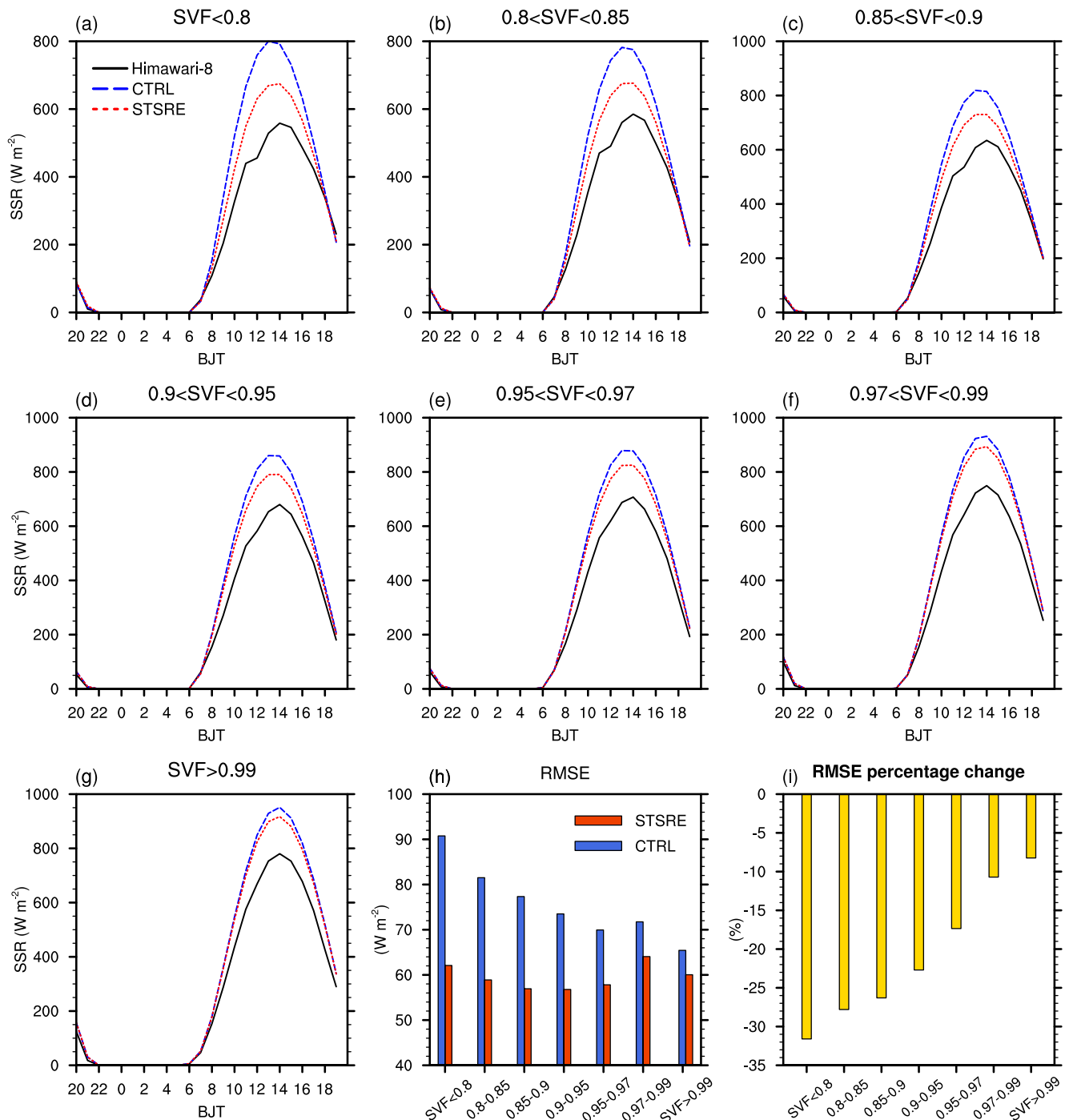
Figure 3. Mean diurnal variations of surface solar radiation (SSR) in June 2020 from the Himawari-8 (black curves), simulations from the CTRL (blue curves) and sub-grid terrain solar radiative effect (STSRE) (red curves) experiments averaged within each category of SVF(a-g). Root mean square errors (RMSEs) for the mean SSR from the CTRL and STSRE experiments relative to the Himawari-8 observation averaged within each category of SVF in June 2020 (h). The RMSE percentage change (STSRE-CTRL/CTRL) for the mean SSR produced by the STSRE experiment relative to the CTRL experiment averaged within each category of SVF in June 2020 (i).

at 12:00 BJT and a RMSE of $\sim$91 W·m^{-2} compared to the observation, and the maximal diurnal bias (RMSE) is largely reduced to $\sim$175 W·m^{-2} ($\sim$62 W·m^{-2}) in the STSRE experiment (Figures 3a and 3h). It could also be found that the RMSEs for the CTRL and STSRE experiments are not monotonical over relatively flat regions starting from SVF >0.95 (Figure 3h). This indicates that the RMSE of SSR simulation is more subjected to the
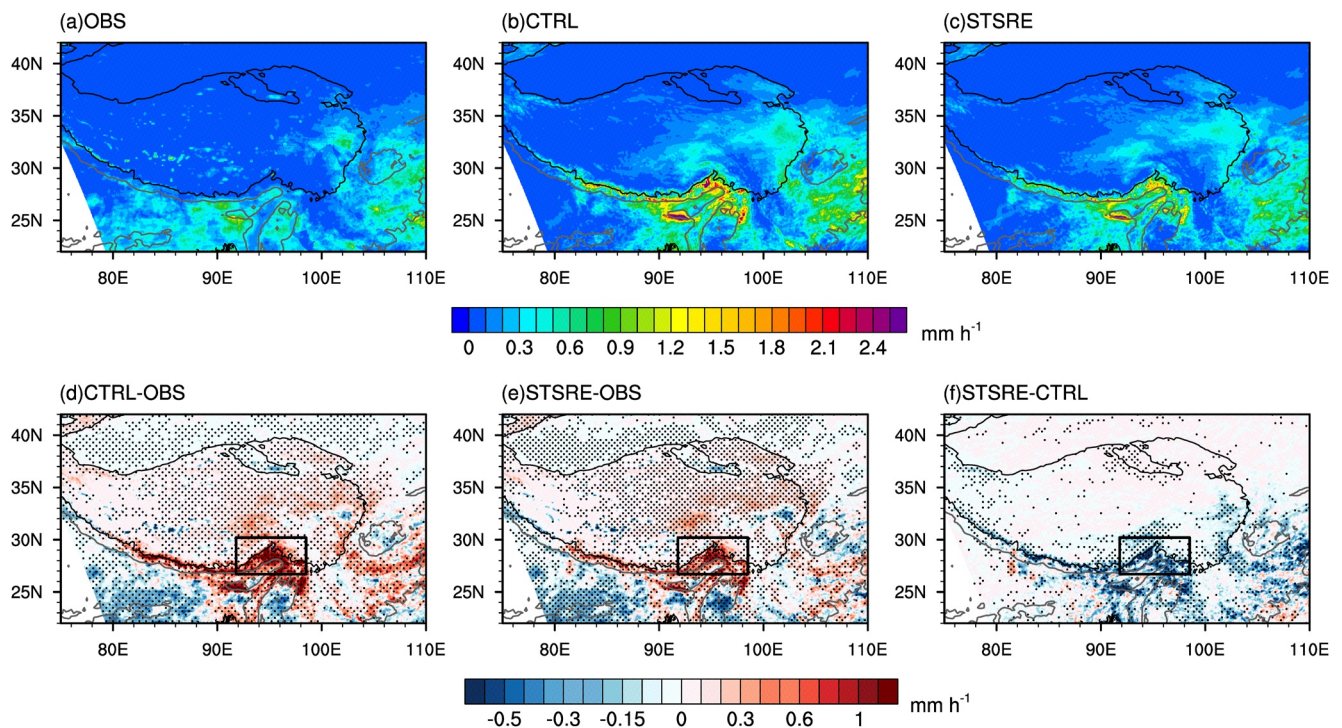
Figure 4. The spatial distributions of mean precipitation in June 2020 from the OBS (a), CTRL (b) and STSRE (c) experiments with the differences between CTRL and OBS (d), between sub-grid terrain solar radiative effect (STSRE) and OBS (e) and between STSRE and CTRL (f). The black (gray) lines denote the terrain height of 3,000 (500) m and the black rectangles sketch the sub-region with much larger differences. The dots indicate the differences over 95% significant confidence level of t test.

sub-grid topographic inhomogeneity under SVF <0.95. But for the cases with the SVF >0.95, the RMSE of the SSR produced by the CTRL and STSRE experiments becomes more erratic with SVF, likely due to the complicated effects of the land-atmosphere interactions on the large number of scattered-distributed grid points over these flat regions (not shown). Overall, the inclusion of 3D STSRE scheme can improve the simulation of SSR under all categories of SVF and the improvement is more significant over the regions with more complicated terrains (Figure 3i). Beside the improvement in simulated SSR, the inclusion of 3D STSRE scheme also mitigates the overestimation of surface skin temperature over the north and south edges of TP and Sichuan Basin and the surrounding regions with complex terrain (not shown).

3.2. Precipitation

Figure 4 presents the mean precipitation in June 2020 from observation, forecasts of the two experiments and their differences. As shown in Figure 4a, the observed precipitation increases from northwest to the southeast with two rainfall centers located in the trumpet-shaped region of the southern TP and the southeastern of Sichuan Basin. Compared to the observation, the two experiments can well depict the precipitation pattern and maximal centers, but both show overestimation in the magnitude of rainfall, especially over the southern TP (Figures 4b and 4c). The adoption of 3D STSRE scheme significantly undermines the excessive rainfall over most regions in the CTRL experiment and reduces the positive biases by 30.2% over the whole TP (Figure 4e). Two obvious weakening centers locate on the southeast of Sichuan Basin and the southern TP with the intensity exceeding -0.6 mm·hr^{-1}. Slightly increased precipitation in the STSRE experiment relative to the CTRL experiment is observed along the margin of the southern slope of TP and southeast of the focused area (Figure 4e).

Figure 5 presents the mean ETS and FBIAS scores of 12-hr accumulated rainfall for each experiment over the whole domain. For the two thresholds of 0.1 and 10 mm, the ETS scores in the STSRE experiment are clearly higher than those of the CTRL experiment (Figures 5a and 5b). The inclusion of 3D STSRE scheme clearly reduces the FBIAS in the CTRL experiment, particularly at the threshold of 10 mm (Figure 5d). This is corresponding to the subjective comparison of rainfall in Figure 4e, which indicates that the overestimated rainfall over the southern TP and the southeast of Sichuan Basin are obviously reduced by the adoption of STSRE scheme.
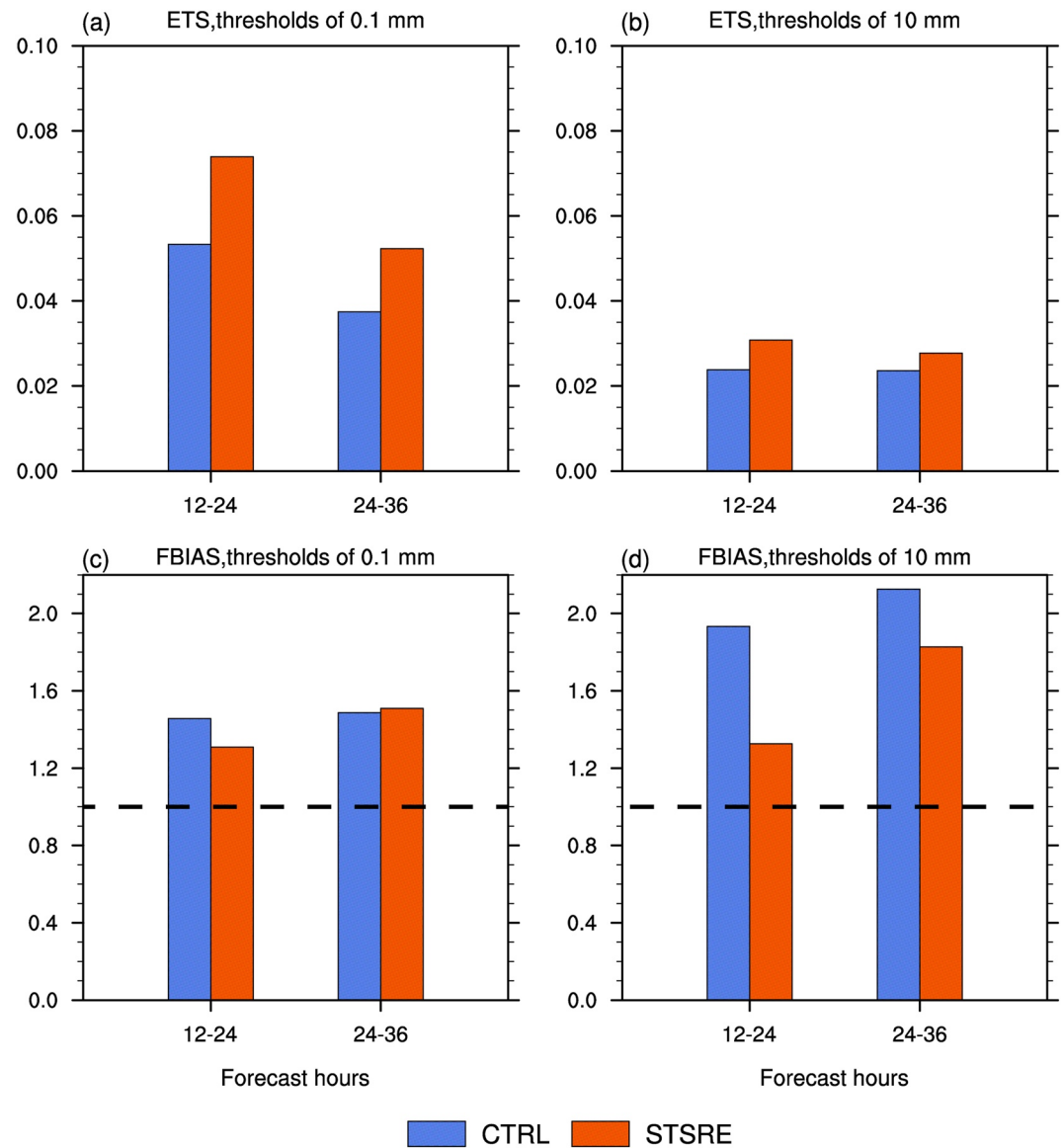
Figure 5. Mean equitable threat score and frequency bias scores of 12-hr accumulated precipitation with thresholds of 0.1 mm (a and b) and 10 mm (c and d) over the whole domain in June 2020. The black dashed lines in (c and d) denote the reference line of 1.0.

Overall, the forecasts in SSR and precipitation can be clearly improved over the TP by introducing the 3D STSRE scheme into the WRF_CPM model, especially over the regions with steep terrains.

4. Discussion

4.1. Impacts of 3D STSRE on Surface Heat

As mentioned above, the adoption of 3D STSRE scheme decreases the SSR, which would influence the surface energy and heat exchanges (Gu et al., 2022; X. Zhang et al., 2022). Apart from surface radiation processes, the surface energy balance is also subjected to the sensible heat, latent heat, and the ground soil heat (soil heat energy change between soil and the ground layer), which can be written as $NR = SH + LH + GFLX$. Here, $NR = NSW - NLW$ represents the surface net radiation flux. NSW is net shortwave flux and NLW is net long-wave flux. LH, SH and GFLX denote the latent heat flux, sensible heat flux and the ground soil heat. NLW, SH and LH are positive upward, while NR, NSW and GFLX are positive downward. Figure 6 shows the differences
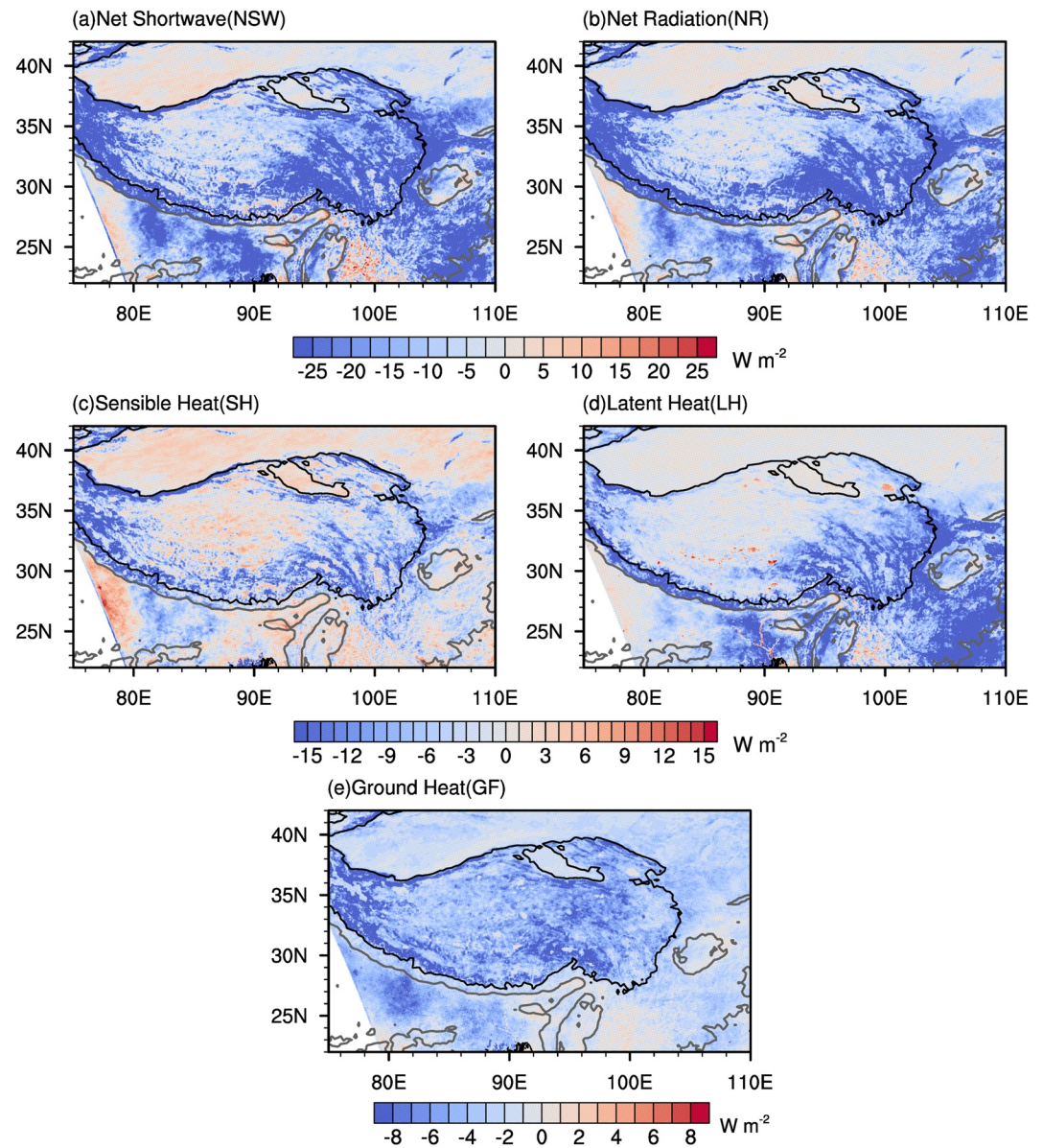
Figure 6. The mean differences of the surface radiation and heat fluxes between the sub-grid terrain solar radiative effect experiment and CTRL experiment in June 2020. The black (gray) lines denote the terrain height of 3,000 (500) m.

in the above heat and radiation fluxes between the STSRE experiment and CTRL experiment. Similar to the SSR in Figure 2f, the application of 3D STSRE scheme diminishes the overestimated NSW over almost the whole region, particularly along steep mountainous regions (e.g., the Hengduan mountains, the Himalayas and mountainous areas surrounds the Sichuan Basin) with values up to ~25 W·m^{-2} (Figure 6a). The magnitude of NLW is much smaller than that of the NSW, which implies the change of mean radiation flux is principally dependent on the shortwave radiation in daytime (not shown). Thus, the spatial pattern of NR resembles that of the NSW (Figure 6b). The negative differences of latent heat and sensible heat can also be observed in the eastern and southern margins along the TP with the magnitude of about −15 W·m^{-2} (Figures 6c and 6d). Compared to the differences of the above surface energy and heat components, the difference in ground heat flux between the two experiments is not evident, ranging from −8 to 4 W·m^{-2} (Figure 6e).

To quantify the magnitude of each component, the regionally averaged surface radiation and heat fluxes of the STSRE and CTRL experiments with their differences are examined. The domain-averaged NSW is over 210 W·m^{-2} in both experiments (Figure 7a) and plays a dominant role in the left side of the equation of surface energy
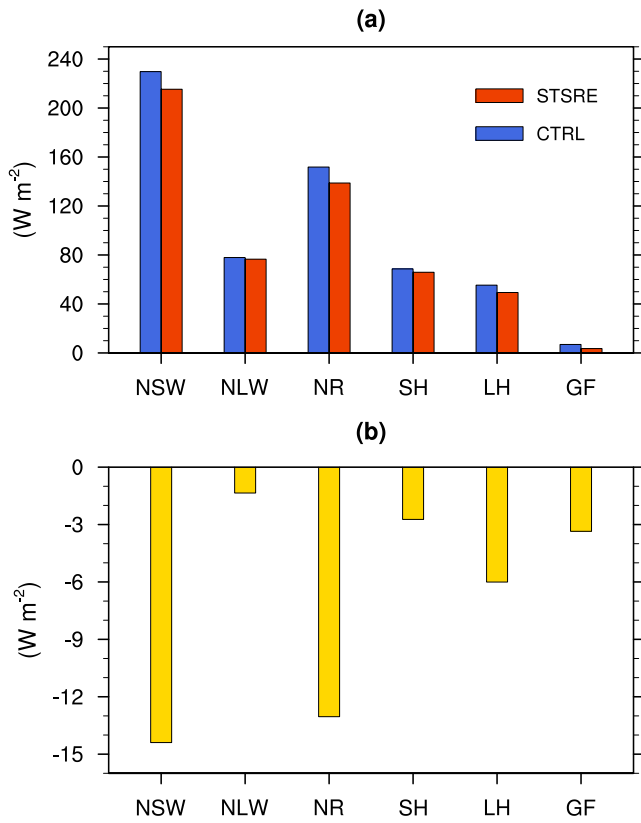
Figure 7. The domain-averaged surface heat balance components from the simulations of the CTRL experiment and sub-grid terrain solar radiative effect (STSRE) experiment in June 2020 (a). The differences of each component between the STSRE experiment and the CTRL experiment in June 2020 (b).

balance. When incorporating the 3D STSRE scheme, the domain-averaged NSW decreased by 14.4 W·m^{-2} exhibits the largest change among all surface heat flux components. The difference in NLW is much smaller with an intensity of -1.4 W · m^{-2} (Figure 7b). For the right hand of the surface energy balance equation, the regionally averaged SH and LH are comparable with the intensity around 60~70 W·m^{-2}, while ground heat flux is only about ~5 W · m^{-2} (Figure 7a). Among three surface heat flux components, the difference in LH is the largest with an intensity of -6.0 W·m^{-2}, implying that the reduction of the NR in the STSRE experiment is primarily compensated by the LH (Figure 7b). Since the LH is relevant to the phase transition of water, this large decreasing of LH coheres with the substantial decreasing of precipitation (Figures 4f and 7b). Overall, the incorporation of 3D STSRE scheme reduces the surface radiation and heat fluxes, resulting in a weaker surface heating. It can be noted that the difference of the surface radiation flux on the left side of the surface energy balance equation is not equal to the surface heat flux of the right, which is mainly due to the interactions among the plant canopy, the atmosphere and the soil layer (Chen & Dudhia, 2001).

4.2. Possible Mechanisms for the Improvement of Precipitation Forecast

By incorporating the 3D STSRE scheme into the WRF_CPM model, the overestimation of SSR in the CTRL experiment is obviously reduced and the precipitation forecast is clearly improved especially over the southern TP. In this subsection, the possible mechanism how the improved SSR affects the precipitation forecast is investigated. Here, the sub-region marked as rectangles in Figures 4d and 4e, where the largest precipitation difference between the STSRE and the CTRL experiments is selected. Yao et al. (2017) showed that the sub-region is influenced by the India summer monsoon and the westerly. The background circulation as well as the local vertical motion and thermal condition from the two experiments are compared and discussed in the following sections.

4.2.1. Background Circulation

During the summer period, the atmospheric heating generates a positive vortex source in the low troposphere, resulting in a stable cyclonic circulation on TP (G. X. Wu et al., 2002). Figure 8 shows the temperature and wind field and their difference between STSRE and CTRL experiments. At 14:00 BJT, there exist thermal-low pressures over the central TP in both experiments. One branch of the airflow comes from the west and flows into the northern TP. The other branch encounters the southern TP from the southwest, providing warm and moist water vapor to the sub-region marked in blue rectangles (Figures 8a and 8b). The temperature difference between the two experiments is the largest compared to other time of a day (Figure 8c). Then, at 20:00 BJT, the intensity of thermal-lows enhances in both experiments (Figures 8d and 8e). The westerly over the northern TP turns to northeasterly winds and the two branches converge at the central TP motivated by the intense thermal-low (Figures 8d and 8e).

By 02:00 BJT, though the thermal-low weakens, easterly winds pools into the northern TP and southwesterly winds come from the southern TP, both contribute to a cyclonic circulation with associated convergence (Figures 8g and 8h). It is notable that the southwesterly winds directing into the sub-region are much stronger at 20:00 BJT-02:00 BJT compared to other times, which is related to the occurrence of the cyclonic circulation over the central TP in both experiments (Figures 8d and 8e and 8g and 8h). Correspondingly, more moisture flux is transported into that sub-region and the diurnal precipitation peak occurs during night (not shown). With the inclusion of the 3D STSRE, the difference in wind field turns to anticyclonic and the water vapor transportation into the sub-region is depressed during 20:00 BJT-02:00 BJT (Figures 8f and 8i). At 08:00 BJT, the cyclonic circulation vanishes and westerly winds flows into the central TP in both experiments (Figures 8j and 8k). The temperature difference is not evident and the anticyclonic difference of wind field disappears between the STSRE experiment and CTRL experiment (Figure 8l).
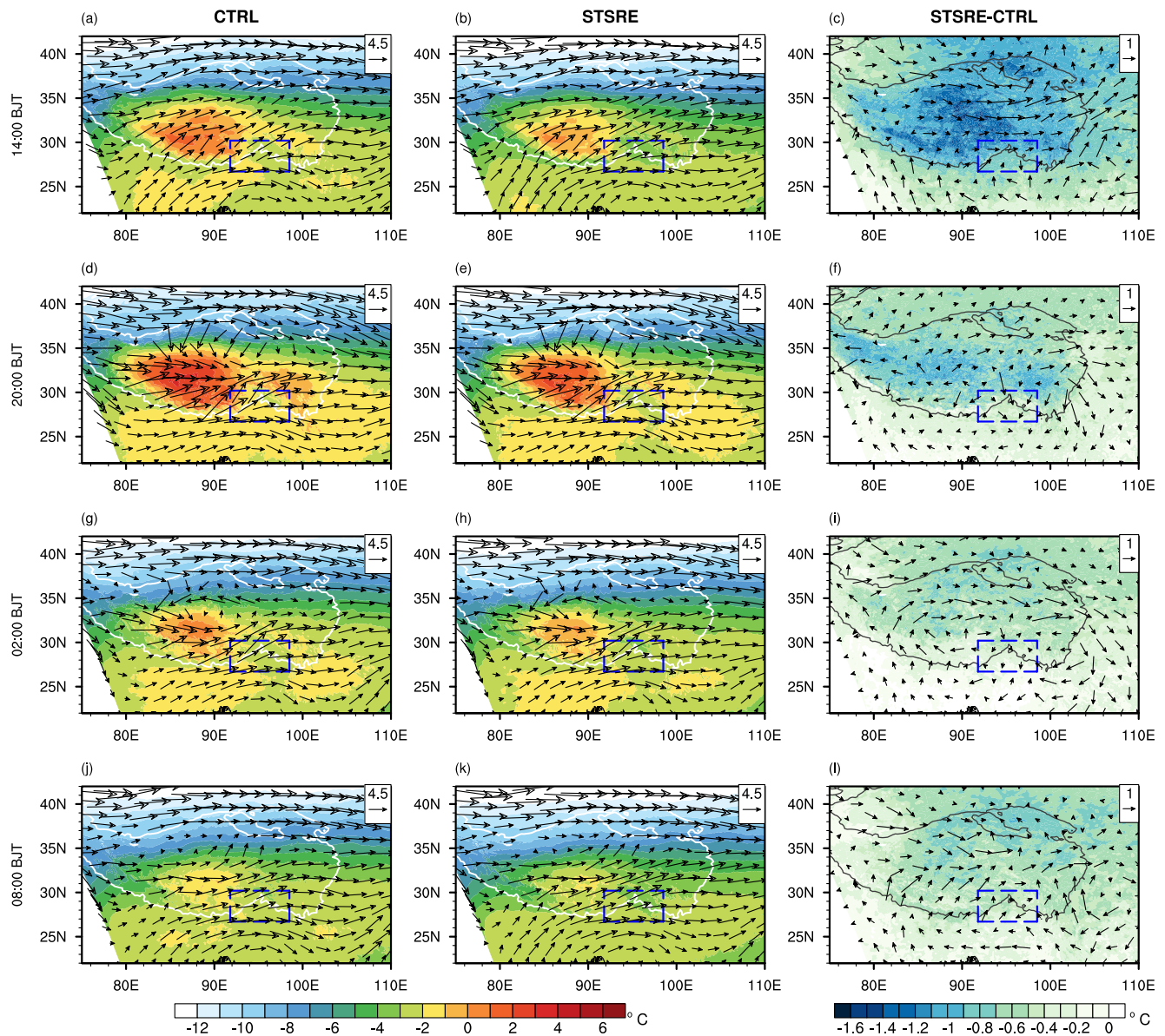
Figure 8. The spatial distribution of the hourly wind field (vectors, units: m s⁻¹) and temperature (shadings, units: °C) at 500 hPa from the CTRL and sub-grid terrain solar radiative effect (STSRE) experiment and their differences (STSRE-CTRL) in June 2020. The white (gray) lines denote the terrain height of 3,000 m and the blue dashed rectangles sketch the sub-region shown in Figures 4d and 4e. The rows are for 14:00 BJT, 20:00 BJT, 02:00 BJT and 08:00 BJT, respectively.

In general, the thermal-low is strong during afternoon to early night and motivates a cyclonic circulation at late night over the TP. Influenced by the cyclonic circulation, the southwesterly winds flowing into the sub-region is more intense at night, which conveys moisture to the sub-region and promotes the precipitation there. The adoption of the 3D STSRE scheme attenuates the thermal-low by reducing the surface thermal forcing. Then, the cyclonic circulation weakens with much weaker peripheral southwesterly winds and less water vapor transportation to the sub-region (Figures 8f and 8i). Hence, the precipitation is depressed. In the morning, the difference of temperature between the two experiments is small but the southwesterly winds are still weaker in the STSRE experiment, which also lead to less water vapor transported to the sub-region and cause less precipitation.

To better understand the difference of the moisture transport to the sub-region between the two experiments, we perform a moisture budget analysis. Figure 9 displays the mean precipitation rate and the moisture budget components regionally averaged over the sub-region from the two experiments during day and night in June 2020. The primary rainfall diurnal peak emerges around 04:00 BJT and the other peak occurs at 14:00 BJT
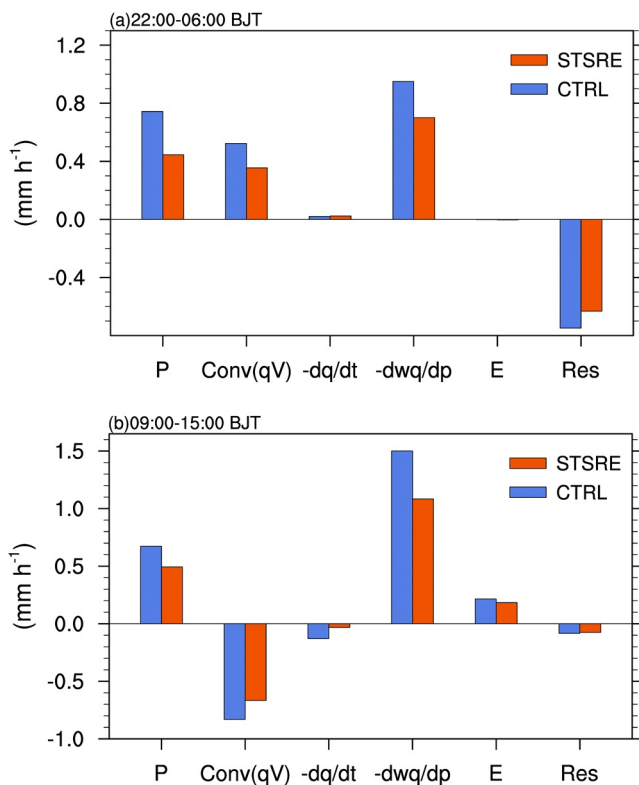
Figure 9. The mean precipitation and moisture budget components during 22:00 ~ 06:00 BJT (a) and 09:00 ~ 15:00 BJT (b) from the CTRL and sub-grid terrain solar radiative effect (STSRE) experiments regionally averaged in the sub-region in June 2020. Here, P and E denote the precipitation and evaporation rate. The "Conv(qV)" is convergence of vertically integrated moisture flux, "$-dq/dt$" indicates the changes of local moisture, "$-dwq/dp$" is the vertical transport of moisture flux. "Res" denotes the residual term.

(figure not shown). The inclusion of 3D STSRE reduces the magnitude of precipitation through the whole day, but the main factors that influence the moisture supply differ in each period. During 22:00 BJT ~ 06:00 BJT, the decrease of precipitation in the STSRE experiment (-0.30 mm $\cdot$ hr^{-1}) is mainly compensated by the weakened convergence of moisture flux (-0.17 mm $\cdot$ hr^{-1}) and vertical transport of moisture flux (-0.25 mm $\cdot$ hr^{-1}) in the sub-region (Figure 9a). This is corresponding to the reduced thermal-low and peripheral southwesterly winds during night in the STSRE experiment (Figures 8g–8i).

In the afternoon, the reduction of precipitation (-0.19 mm $\cdot$ hr^{-1}) is contributed by the less evaporation (-0.03 mm $\cdot$ hr^{-1}) and weaker vertical moisture transport (-0.41 mm$\cdot$hr^{-1}; Figure 9b), which is related to the decreased surface skin temperature and weaker upward motion in the STSRE experiment respectively. We can infer that the decrease of the afternoon rainfall in the STSRE experiment mainly results from the weaker local solar heating. This will be discussed in Section 4.2.2.

Overall, adopting the 3D STSRE scheme leads to the decrease of the surface heating. Influenced by the weaker surface heating, the thermal-low over the central TP is attenuated and the peripheral southwesterly winds motivated by the thermal-low also weaken in the STSRE experiment. Thus, the convergence of moisture flux in the sub-region is weaker in the STSRE experiment, especially during night (Figures 8i and 9a). In the afternoon, compared to the CTRL experiment, the surface temperature is lower and less moisture is evaporated. The decreased local surface heating also causes the weaker vertical moisture transport in the STSRE experiment (Figure 9b). Therefore, the precipitation is reduced over the sub-region in the STSRE experiment (Figures 4e and 9b).

4.2.2. Local Thermal Conditions

Previous studies have shown that the annual rainfall of the sub-region is primarily composed of convective precipitation (Maussion et al., 2014). The local thermo-dynamic conditions play key roles in the formation and evolution of convective precipitation.

Figure 10 gives the spatial distribution of the convective available potential energy (CAPE) in the sub-region to investigate the impacts of 3D STSRE scheme on the local thermal condition. In the both experiments, the CAPE larger than 780 J kg^{-1} exists over the sub-region, which corresponds to the regions with more precipitation (Figures 4a–4c and 10a and 10b). The STSRE experiment produces smaller CAPE over the sub-region, resulting in a much more stable atmospheric condition and weaker upward motion there (Figure 10c). Hence, the development of convection is inhibited, causing less precipitation over the sub-region in the STSRE experiment than in the CTRL experiment (Figure 4e).

The south-north oriented transect of local meridional circulation along with equivalent potential temperature over the sub-region from the two experiments and their differences are presented in Figure 11. Strong upward movement is found in the lower troposphere along 27°–29°N in both experiments, which can trigger local convection (Figures 11a and 11b). The intensive updraft extends to the upper troposphere and the equivalent potential temperature is high along 28°–29°N in the CTRL experiment (Figure 11a). Clearly, the implementation of 3D STSRE scheme reduces the surface heating, leading to more stable atmosphere and weaker upward motion relative to the CTRL experiment (Figure 11c). This corresponds to the weakened vertical moisture transport in Figure 9. Thus, the precipitation is suppressed over the sub-region in the STSRE experiment (Figure 4e).

To sum up, the inclusion of 3D STSRE scheme weakens the surface heating and stabilizes the atmosphere, which leads to weaker upward motion and less active convection over the sub-region. Thus, the total precipitation largely decreases therein.
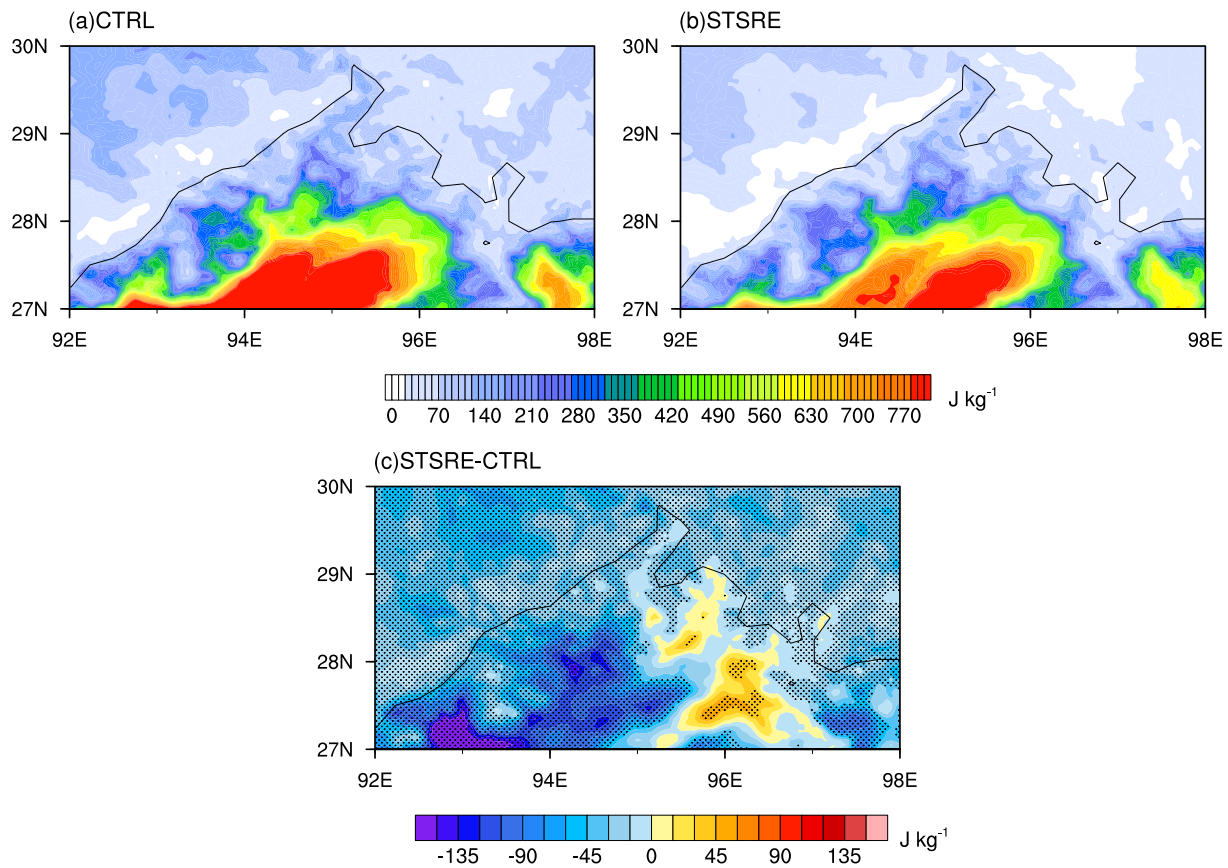
Figure 10. The mean convective available potential energy in June 2020 (shading, units: J kg^{-1}) from the CTRL (a) and sub-grid terrain solar radiative effect (STSRE) (b) experiments, and the difference between the STSRE experiment and CTRL experiment (c) over the sub-region. The black lines denote the terrain height of 3,000 m. The dots indicate the differences over 90% significant confidence level of *t* test.

5. Summary and Discussion

In this study, a 3D STSRE scheme is introduced into the WRF_CPM model to improve the summer rainfall forecast on the TP and surrounding regions featured by complex terrains. Two experiments with and without STSRE are conducted to inspect the effects of the 3D STSRE scheme on the ability of WRF_CPM in forecasting precipitation in summer.

Compared to the CTRL experiment, the application of 3D STSRE largely reduces the overestimation of SSR, especially over the steep terrains with much smaller SVF. The improved SSR in the STSRE experiment influences the surface energy balance, which finally leads to a reduction in the wet biases on the TP. Overall, adopting the 3D STSRE scheme can reduce the overestimation of the mean precipitation over the TP in the CTRL experiment by 30.2%.

Taking a part of the southern TP with complex terrain as a sub-region, we then investigate the possible reasons for the improvement of rainfall forecast. The reduced SSR acts to weaken the surface heating, which results in the attenuated thermal-low over the central TP in the STSRE experiment. Subsequently, the peripheral southwesterly winds around the thermal-low are weakened and the convergence of moisture flux is weaker in the sub-region, especially at night. Also, the reduced SSR results in lower surface skin temperature and weaker upward motion, which accordingly decreases the surface evaporation and vertical moisture transport during daytime. The weakened convergence of moisture flux, vertical moisture transport together with reduction of evaporation in the STSRE experiment eventually alleviate the overestimation of the precipitation in the CTRL experiment. Moreover, the suppressed surface heating stabilizes the local atmosphere and inhibits the convection, which is another reason for the decrease of precipitation over the sub-region.

It should be noted that, the positive bias of SSR in the CTRL experiment is evident over the whole domain, which is a common issue for the current WRF simulations and many CMIP6 model simulations (Z. Gao et al., 2022; He
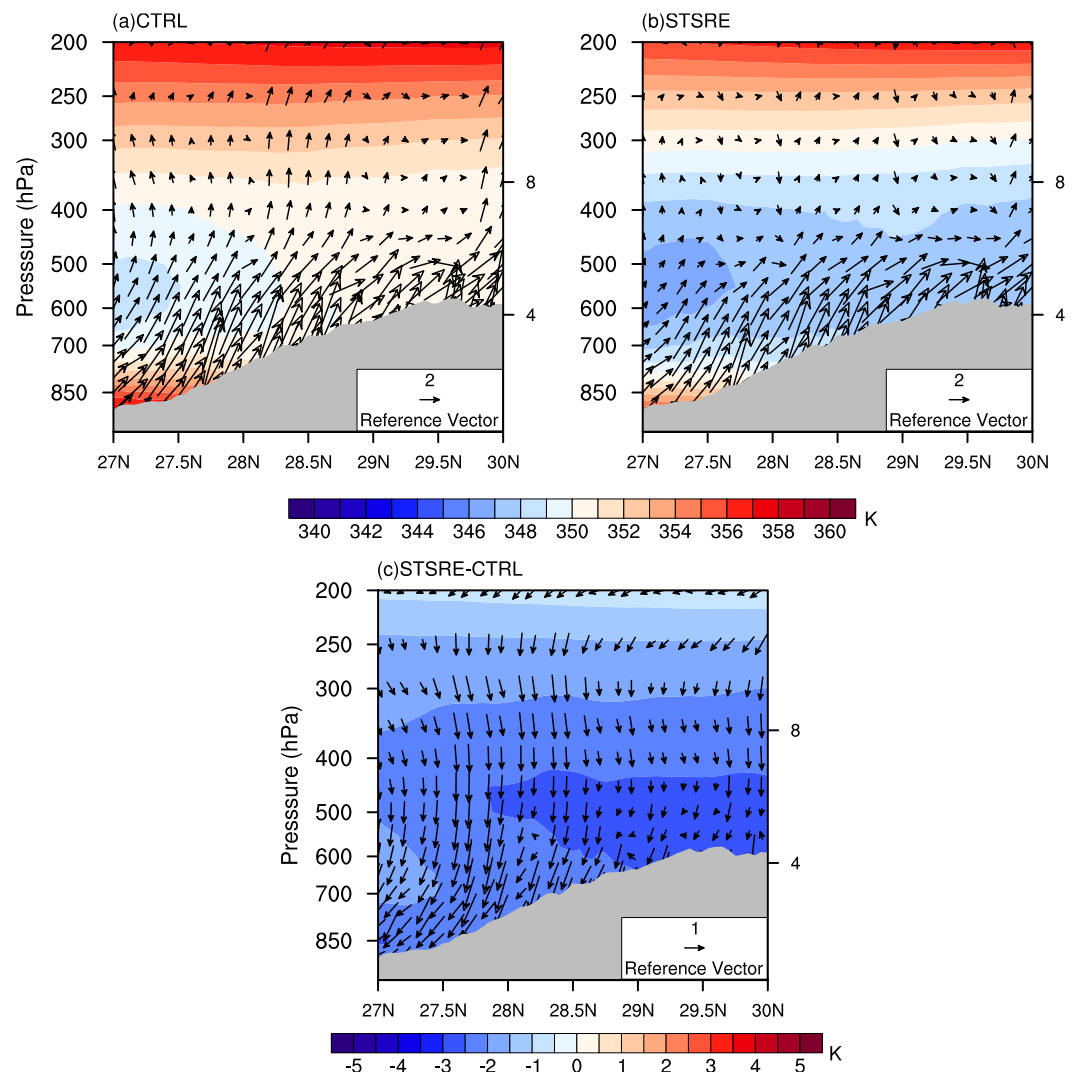
Figure 11. Height-latitude cross section of the mean vertical circulation (units: m s^{-1}; with the vertical velocity scaled by 100) and equivalent potential temperature (shading, units: K) in June 2020 averaged along 92° ∼ 98°E from the CTRL (a) and sub-grid terrain solar radiative effect (STSRE) (b) experiments, and their differences between the STSRE experiment and CTRL experiment (c).

et al., 2023; Yang et al., 2020). Clouds and aerosols are known as the primary sources of model biases of SSR (Boers et al., 2017; Cherian & Quaas, 2020; Moseid et al., 2020). Although we found that the bias of total cloud cover negatively correlates with the bias of SSR over most of the regions, it cannot absolutely explain the SSR bias over the entire domain. In this study, we emphasize the thermal effects of sub-grid topographic inhomogeneity on the SSR and alleviate the overestimation of SSR over steep regions by depicting more realistic terrain and land-surface interaction. In addition, the incorporation of the 3D STSRE scheme in WRF_CPM provides an effective way to promote the precipitation forecast over the regions with complicated terrains. Due to the limitation of computing resource, the short-range forecast of WRF_CPM model is conducted for only 1 month. Clearly, the forecast skill of WRF_CPM model at synoptic time scale obviously improved by adopting the 3D STSRE scheme is encouraging and the results are consistent with previous studies (Gu et al., 2022; Y. Zhang et al., 2006). Subsequent studies on how the 3D STSRE affect the performance of WRF_CPM model at longer time scale are also needed. Additionally, the incorporation of 3D STSRE scheme would influence the atmospheric circulation downstream as the integration time increases (Huang & Qian, 2008). In the future, we will investigate to what extent of the 3D STSRE scheme can affect the synoptic processes downstream and the underlying physical drivers. This may provide another approach to improve the downstream weather prediction in the future.

Data Availability Statement

Datasets—The Shuttle Radar Topography Mission (SRTM) 90m Digital Elevation Database v4.1 is available at https://developers.google.com/earth-engine/datasets/catalog/CGIAR_SRTM90_V4 (Jarvis et al., 2008). The 10-min East Asia-Pacific longwave/shortwave downward radiation at the surface data set is derived from https://doi.org/10.11888/Meteoro.tpdc.271729 (Letu et al., 2022). The hourly precipitation observation is available at http://data.cma.cn/site/index.html (Shen et al., 2014). The 3-hr NCEP Global Forecast System real-time forecasts is obtained from https://rda.ucar.edu/datasets/ds084.1 (NCEP, 2015). Software—The source code of the WRF Preprocessing System Version 4.2 (WPS4.2) and the Weather Research and Forecasting model Version4.2 (WRF4.2) is available at https://doi.org/10.5281/zenodo.7722110 (Cai, 2023a). The codes of the WRF model incorporating with the 3D STSRE scheme are available at https://zenodo.org/record/7722215 (Cai, 2023b). All figures were plotted by NCL V6.6.2 which is available at https://doi.org/10.5065/D6WD3XH5 (NCAR, 2019). The sizes of the two groups of WRF forecasts are very large. Anyone who is interested could request selected variables via email cicicsx@outlook.com.

References

Arnold, N. S., Rees, W. G., Hodson, A. J., & Kohler, J. (2006). Topographic controls on the surface energy balance of a high Arctic valley glacier. *Journal of Geophysical Research*, *111*(F2), F02011. https://doi.org/10.1029/2005jf000426

Arthur, R. S., Lundquist, K. A., Mirocha, J. D., & Chow, F. K. (2018). Topographic effects on radiation in the WRF Model with the immersed boundary method: Implementation, validation, and application to complex terrain. *Monthly Weather Review*, *146*(10), 3277–3292. https://doi.org/10.1175/MWR-D-18-0108.1

Boers, R., Brandsma, T., & Siebesma, A. P. (2017). Impact of aerosols and clouds on decadal trends in all-sky solar radiation over The Netherlands (1966–2015). *Atmospheric Chemistry and Physics*, *17*(13), 8081–8100. https://doi.org/10.5194/acp-17-8081-2017

Brown, B. G., Gotway, J. H., Bullock, R., Gilleland, E., & Ahijevych, D. (2009). The model evaluation Tools (MET): Community tools for forecast evaluation. In *25th Conference on International Interactive Information and Processing Systems (IIPS) for Meteorology, Oceanography, and Hydrology*.

Cai, S. (2023a). The source codes of WRF-V4.2 and WPS-V4.2 [Software]. Zenodo. https://doi.org/10.5281/zenodo.7722110

Cai, S. (2023b). WRF-3D STSRE [Software]. Zenodo. https://doi.org/10.5281/zenodo.7722215

Cai, S., Huang, A., Zhu, K., Yang, B., Yang, X., Wu, Y., & Mu, X. (2021). Diurnal cycle of summer precipitation over the Eastern Tibetan Plateau and surrounding regions simulated in a convection-permitting model. *Climate Dynamics*, *57*(1), 611–632. https://doi.org/10.1007/s00382-021-05729-5

Chen, F., & Dudhia, J. (2001). Coupling an advanced land surface–hydrology model with the Penn State–NCAR MM5 modeling system. Part I: Model implementation and sensitivity. *Monthly Weather Review*, *129*(4), 569–585. https://doi.org/10.1175/1520-0493(2001)129<0569:CAALSH>2.0.CO;2

Chen, Y., Hall, A., & Liou, K. N. (2006). Application of three-dimensional solar radiative transfer to mountains. *Journal of Geophysical Research*, *111*(D21), D21111. https://doi.org/10.1029/2006JD007163

Cherian, R., & Quaas, J. (2020). Trends in AOD, clouds, and cloud radiative effects in satellite data and CMIP5 and CMIP6 model simulations over aerosol source regions. *Geophysical Research Letters*, *47*(9), e2020GL087132. https://doi.org/10.1029/2020GL087132

Choi, H. J., Choi, S. J., Koo, M. S., Kim, J. E., Kwon, Y. C., & Hong, S. Y. (2017). Effects of parameterized orographic drag on weather forecasting and simulated climatology over East Asia during boreal summer. *Journal of Geophysical Research: Atmospheres*, *122*(20), 10–669. https://doi.org/10.1002/2017JD026696

Chou, C., & Lan, C. W. (2012). Changes in the annual range of precipitation under global warming. *Journal of Climate*, *25*(1), 222–235. https://doi.org/10.1175/JCLI-D-11-00097.1

Colette, A., Chow, F. K., & Street, R. L. (2003). A numerical study of inversion-layer breakup and the effects of topographic shading in idealized valleys. *Journal of Applied Meteorology and Climatology*, *42*(9), 1255–1272. https://doi.org/10.1175/1520-0450(2003)042<1255:ANSOIB>2.0.CO;2

Collins, W. D., Rasch, P. J., Boville, B. A., Hack, J. J., McCaa, J. R., Williamson, D. L., et al. (2004). Description of the NCAR community atmosphere model (CAM 3.0). *NCAR Tech. Note NCAR/TN-464+ STR*, *226*, 1326–1334. https://doi.org/10.5065/D63N21CH

Dozier, J., & Frew, J. (1990). Rapid calculation of terrain parameters for radiation modeling from digital elevation data. *IEEE Transactions on Geoscience and Remote Sensing*, *28*(5), 963–969. https://doi.org/10.1109/36.58986

Ebert, E. E., Damrath, U., Wergen, W., & Baldwin, M. E. (2003). Supplement to the WGNE assessment of short-term quantitative precipitation forecasts. *Bulletin of the American Meteorological Society*, *84*(4), ES10–11. https://doi.org/10.1175/bams-84-4-ebert

Gao, Y., Xiao, L., Chen, D., Chen, F., Xu, J., & Xu, Y. (2017). Quantification of the relative role of land-surface processes and large-scale forcing in dynamic downscaling over the Tibetan Plateau. *Climate Dynamics*, *48*(5), 1705–1721. https://doi.org/10.1007/s00382-016-3168-6

Gao, Y. C., & Liu, M. (2013). Evaluation of high-resolution satellite precipitation products using rain gauge observations over the Tibetan Plateau. *Hydrology and Earth System Sciences*, *17*(2), 837–849. https://doi.org/10.5194/hess-17-837-2013

Gao, Z., Zhao, C., Yan, X., Guo, Y., Liu, S., Luo, N., et al. (2022). Effects of cumulus and radiation parameterization on summer surface air temperature over eastern China. *Climate Dynamics*, 1–19. https://doi.org/10.1007/s00382-022-06601-w

Gu, C., Huang, A., Wu, Y., Yang, B., Mu, X., Zhang, X., & Cai, S. (2020). Effects of subgrid terrain radiative forcing on the ability of RegCM4.1 in the simulation of summer precipitation over China. *Journal of Geophysical Research: Atmospheres*, *125*(12), e2019JD032215. https://doi.org/10.1029/2019jd032215

Gu, C., Huang, A., Zhang, Y., Yang, B., Cai, S., Xu, X., et al. (2022). The wet bias of RegCM4 over Tibet Plateau in summer reduced by adopting the 3D sub-grid terrain solar radiative effect parameterization scheme. *Journal of Geophysical Research: Atmosphere*, *127*(21). https://doi.org/10.1029/2022JD037434

Gu, Y., Liou, K. N., Lee, W. L., & Leung, L. R. (2012). Simulating 3-D radiative transfer effects over the Sierra Nevada Mountains using WRF. *Atmospheric Chemistry and Physics*, *12*(20), 9965–9976. https://doi.org/10.5194/acp-12-9965-2012

Hao, D., Bisht, G., Gu, Y., Lee, W. L., Liou, K. N., & Leung, L. R. (2021). A parameterization of sub-grid topographical effects on solar radiation in the E3SM Land Model (version 1.0): Implementation and evaluation over the Tibetan Plateau. *Geoscientific Model Development*, *14*(10), 6273–6289. https://doi.org/10.5194/gmd-14-6273-2021

Hao, D., Bisht, G., Huang, M., Ma, P. L., Tesfa, T., Lee, W. L., et al. (2022). Impacts of sub-grid topographic representations on surface energy balance and boundary conditions in the E3SM land model: A case study in Sierra Nevada. *Journal of Advances in Modeling Earth Systems*, *14*(4), e2021MS002862. https://doi.org/10.1029/2021MS002862

Hauge, G., & Hole, L. R. (2003). Implementation of slope irradiance in Mesoscale Model version 5 and its effect on temperature and wind fields during the breakup of a temperature inversion. *Journal of Geophysical Research*, *108*(D2), 4058. https://doi.org/10.1029/2002jd002575

He, Y., Yang, K., Wild, M., Wang, K., Tong, D., Shao, C., & Zhou, T. (2023). Constrained future brightening of solar radiation and its implication for China's solar power. *National Science Review*, *10*(1), nwac242. https://doi.org/10.1093/nsr/nwac242

Helbig, N., & Löwe, H. (2012). Shortwave radiation parameterization scheme for subgrid topography. *Journal of Geophysical Research*, *117*(D3). https://doi.org/10.1029/2011JD016465

Hock, R., & Holmgren, B. (2005). A distributed surface energy-balance model for complex topography and its application to Storglaciären, Sweden. *Journal of Glaciology*, *51*(172), 25–36. https://doi.org/10.3189/172756505781829566

Hong, S. Y., Dudhia, J., & Chen, S. H. (2004). A revised approach to ice microphysical processes for the bulk parameterization of clouds and precipitation. *Monthly Weather Review*, *132*(1), 103–120. https://doi.org/10.1175/1520-0493(2004)132<0103:ARATIM>2.0.CO;2

Hong, S. Y., Noh, Y., & Dudhia, J. (2006). A new vertical diffusion package with an explicit treatment of entrainment processes. *Monthly Weather Review*, *134*(9), 2318–2341. https://doi.org/10.1175/MWR3199.1

Huang, A., Gu, C., Zhang, Y., Li, W., Zhang, L., Wu, Y., et al. (2022). Development of a clear-sky 3D sub-grid terrain solar radiative effect parameterization scheme based on the mountain radiation theory. *Journal of Geophysical Research: Atmospheres*, *127*(13), e2022JD036449. https://doi.org/10.1029/2022JD036449

Huang, D. Q., & Qian, Y. F. (2008). The effects of the slope irradiance on different weather processes under different model resolutions. *Acta Meteorologica Sinica*, *66*(1), 90–100. (in Chinese). https://doi.org/10.11676/qxxb2008.009

Jarvis, A., Reuter, H. I., Nelson, A., & Guevara, E. (2008). Hole-filled SRTM for the globe version 4. [Dataset]. International Centre for Tropical Agriculture (CIAT). Retrieved from http://srtm.csi.cgiar.org

Jiménez, P. A., & Dudhia, J. (2013). On the ability of the WRF model to reproduce the surface wind direction over complex terrain. *Journal of Applied Meteorology and Climatology*, *52*(7), 1610–1617. https://doi.org/10.1175/JAMC-D-12-0266.1

Joyce, R. J., Janowiak, J. E., Arkin, P. A., & Xie, P. (2004). CMORPH: A method that produces global precipitation estimates from passive microwave and infrared data at high spatial and temporal resolution. *Journal of Hydrometeorology*, *5*(3), 487–503. https://doi.org/10.1175/1525-7541(2004)005<0487:CAMTPG>2.0.CO;2

Kan, M., Huang, A., Zhao, Y., Zhou, Y., Yang, B., & Wu, H. (2015). Evaluation of the summer precipitation over China simulated by BCC_CSM model with different horizontal resolutions during the recent half century. *Journal of Geophysical Research: Atmospheres*, *120*(10), 4657–4670. https://doi.org/10.1002/2015JD023131

Kim, Y. J., & Doyle, J. D. (2005). Extension of an orographic-drag parametrization scheme to incorporate orographic anisotropy and flow blocking. *Quarterly Journal of the Royal Meteorological Society*, *131*(609), 1893–1921. https://doi.org/10.1256/qj.04.160

Kondrat'yev, K. Y. (1965). *Radiative heat exchange in the atmosphere (translated from the Russian by O. Tedder* (p. 332). Pergamon Press. https://doi.org/10.1016/C2013-0-05325-X

Lee, W. L., Gu, Y., Liou, K. N., Leung, L. R., & Hsu, H. H. (2015). A global model simulation for 3-D radiative transfer impact on surface hydrology over the Sierra Nevada and Rocky Mountains. *Atmospheric Chemistry and Physics*, *15*(10), 5405–5413. https://doi.org/10.5194/acp-15-5405-2015

Lee, W. L., Liou, K. N., & Hall, A. (2011). Parameterization of solar fluxes over mountain surfaces for application to climate models. *Journal of Geophysical Research*, *116*(D1), D01101. https://doi.org/10.1029/2010JD014722

Lee, W. L., Liou, K. N., Wang, C. C., Gu, Y., Hsu, H. H., & Li, J. L. F. (2019). Impact of 3-D radiation-topography interactions on surface temperature and energy budget over the Tibetan Plateau in winter. *Journal of Geophysical Research: Atmospheres*, *124*(3), 1537–1549. https://doi.org/10.1029/2018JD029592

Letu, H., Nakajima, T. Y., Wang, T., Shang, H., Ma, R., Yang, K., et al. (2022). A new benchmark for surface radiation products over the East Asia–Pacific region retrieved from the Himawari-8/AHI next-generation geostationary satellite [Dataset]. Bulletin of the American Meteorological Society, *103*(3), E873–E888. https://doi.org/10.1175/BAMS-D-20-0148.1

Li, J., & Luo, J. (2015). Estimation of solar radiation over rugged terrains based on clear sky condition. *Arid Land Geography*, *38*(1), 120–127. (in Chinese with English abstract).

Li, P., Furtado, K., Zhou, T., Chen, H., & Li, J. (2021). Convection-permitting modelling improves simulated precipitation over the central and eastern Tibetan Plateau. *Quarterly Journal of the Royal Meteorological Society*, *147*(734), 341–362. https://doi.org/10.1002/qj.3921

Li, P., Furtado, K., Zhou, T., Chen, H., Li, J., Guo, Z., & Xiao, C. (2020). The diurnal cycle of East Asian summer monsoon precipitation simulated by the Met Office Unified Model at convection-permitting scales. *Climate Dynamics*, *55*(1–2), 131–151. https://doi.org/10.1007/s00382-018-4368-z

Lin, C., Chen, D., Yang, K., & Ou, T. (2018). Impact of model resolution on simulating the water vapor transport through the central Himalayas: Implication for models' wet bias over the Tibetan Plateau. *Climate Dynamics*, *51*(9), 3195–3207. https://doi.org/10.1007/s00382-018-4074-x

Lin, R., Zhou, T., & Qian, Y. (2014). Evaluation of global monsoon precipitation changes based on five reanalysis datasets. *Journal of Climate*, *27*(3), 1271–1289. https://doi.org/10.1175/JCLI-D-13-00215.1

Lindvall, J., Svensson, G., & Hannay, C. (2013). Evaluation of near-surface parameters in the two versions of the atmospheric model in CESM1 using flux station observations. *Journal of Climate*, *26*(1), 26–44. https://doi.org/10.1175/Jcli-D-12-00020.1

Liou, K. N., Gu, Y., Leung, L. R., Lee, W. L., & Fovell, R. G. (2013). A WRF simulation of the impact of 3-D radiative transfer on surface hydrology over the Rocky Mountains and Sierra Nevada. *Atmospheric Chemistry and Physics*, *13*(23), 11709–11721. https://doi.org/10.5194/acp-13-11709-2013

Liou, K. N., Lee, W.-L., & Hall, A. (2007). Radiative transfer in mountains: Application to the Tibetan plateau. *Geophysical Research Letters*, *34*(23), L23809. https://doi.org/10.1029/2007gl031762

Ma, S., & Zhou, T. (2015). Precipitation changes in wet and dry seasons over the 20th century simulated by two versions of the FGOALS model. *Advances in Atmospheric Sciences*, *32*(6), 839–854. https://doi.org/10.1007/s00376-014-4136-x

Manners, J., Vosper, S. B., & Roberts, N. (2012). Radiative transfer over resolved topographic features for high-resolution weather prediction. *Quarterly Journal of the Royal Meteorological Society*, *138*(664), 720–733. https://doi.org/10.1002/qj.956

Maussion, F., Scherer, D., Mölg, T., Collier, E., Curio, J., & Finkelnburg, R. (2014). Precipitation seasonality and variability over the Tibetan plateau as resolved by the high Asia reanalysis. *Journal of Climate*, *27*(5), 1910–1927. https://doi.org/10.1175/JCLI-D-13-00282.1

McFarlane, N. A. (1987). The effect of orographically excited gravity wave drag on the general circulation of the lower stratosphere and troposphere. *Journal of the Atmospheric Sciences*, *44*(14), 1775–1800. https://doi.org/10.1175/1520-0469(1987)044<1775:TEOOEG>2.0.CO;2

Mesinger, F., & Black, T. L. (1992). On the impact on forecast accuracy of the step-mountain (eta) vs. sigma coordinate. *Meteorology and Atmospheric Physics*, *50*(1–3), 47–60. https://doi.org/10.1007/BF01025504

Moseid, K. O., Schulz, M., Storelvmo, T., Julsrud, I. R., Olivié, D., Nabat, P., et al. (2020). *Bias in CMIP6 models compared to observed regional dimming and brightening trends (1961-2014) (No. EGU2020-3349)*. Copernicus Meetings. https://doi.org/10.5194/acp-2019-1210

Müller, M. D., & Scherer, D. (2005). A grid- and subgrid-scale radiation parameterization of topographic effects for mesoscale weather forecast models. *Monthly Weather Review*, *133*(6), 1431–1442. https://doi.org/10.1175/mwr2927.1

NCAR. (2019). The NCAR Command Language (version 6.6.2). [Software]. UCAR/NCAR/CISL/TDD. https://doi.org/10.5065/D6WD3XH5

NCEP (2015). NCEP GFS 0.25° global forecast grids historical Archive. [Dataset]. Retrieved from https://rda.ucar.edu/datasets/ds084.1/

Prein, A. F., Langhans, W., Fosser, G., Ferrone, A., Ban, N., Goergen, K., et al. (2015). A review on regional convection-permitting climate modeling: Demonstrations, prospects, and challenges. *Reviews of Geophysics*, *53*(2), 323–361. https://doi.org/10.1002/2014RG000475

Qiu, J. (2008). China: The third pole. *Nature*, *454*(7203), 393–396. https://doi.org/10.1038/454393a

Seager, R., Naik, N., & Vecchi, G. A. (2010). Thermodynamic and dynamic mechanisms for large-scale changes in the hydrological cycle in response to global warming. *Journal of Climate*, *23*(17), 4651–4668. https://doi.org/10.1175/2010JCLI3655.1

Shen, Y., Xiong, A., Wang, Y., & Xie, P. (2010). Performance of high-resolution satellite precipitation products over China. *Journal of Geophysical Research*, *115*(D2), D02114. https://doi.org/10.1029/2009JD012097

Shen, Y., Zhao, P., Pan, Y., & Yu, J. (2014). A high spatiotemporal gauge-satellite merged precipitation analysis over China [Dataset]. Journal of Geophysical Research: Atmospheres, *119*(6), 3063–3075. https://doi.org/10.1002/2013JD020686

Skamarock, W. C., Klemp, J. B., Dudhia, J., Gill, D. O., Liu, Z., Berner, J., et al. (2019). *A description of the advanced research WRF model version 4* (Vol. 145, p. 145). National Center for Atmospheric Research.

Wang, C. C. (2014). On the calculation and correction of equitable threat score for model quantitative precipitation forecasts for small verification areas: The example of Taiwan. *Weather and Forecasting*, *29*(4), 788–798. https://doi.org/10.1175/WAF-D-13-00087.1

Wang, X., Pang, G., & Yang, M. (2018). Precipitation over the Tibetan plateau during recent decades: A review based on observations and simulations. *International Journal of Climatology*, *38*(3), 1116–1131. https://doi.org/10.1002/joc.5246

Wang, Y., Yang, K., Zhou, X., Chen, D., Lu, H., Ouyang, L., et al. (2020). Synergy of orographic drag parameterization and high resolution greatly reduces biases of WRF-simulated precipitation in central Himalaya. *Climate Dynamics*, *54*(3), 1729–1740. https://doi.org/10.1007/s00382-019-05080-w

Weisman, M. L., Skamarock, W. C., & Klemp, J. B. (1997). The resolution dependence of explicitly modeled convective systems. *Monthly Weather Review*, *125*(4), 527–548. https://doi.org/10.1175/1520-0493(1997)125<0527:TRDOEM>2.0.CO;2

Wooding, R. A., Bradley, E. F., & Marshall, J. K. (1973). Drag due to regular arrays of roughness elements of varying geometry. *Boundary-Layer Meteorology*, *5*(3), 285–308. https://doi.org/10.1007/BF00155238

Wu, G. X., & Chen, S. J. (1985). The effect of mechanical forcing on the formation of a mesoscale vortex. *Quarterly Journal of the Royal Meteorological Society*, *111*(470), 1049–1070. https://doi.org/10.1256/smsqj.47008

Wu, G. X., Liu, X., Zhang, Q., Qian, Y., Mao, J., Liu, Y., & Li, W. (2002). Progresses in the study of the climate impacts of the elevated heating over the Tibetan Plateau. *Environmental Research: Climate*, *7*(2), 184–200. (in Chinese). https://doi.org/10.3969/j.issn.1006-9585.2002.02.006

Wu, Y., Huang, A., Huang, D., Chen, F., Yang, B., Zhou, Y., et al. (2018). Diurnal variations of summer precipitation over the regions east to Tibetan Plateau. *Climate Dynamics*, *51*(11), 4287–4307. https://doi.org/10.1007/s00382-017-4042-x

Xu, J., Koldunov, N., Remedio, A. R. C., Sein, D. V., Zhi, X., Jiang, X., et al. (2018). On the role of horizontal resolution over the Tibetan Plateau in the REMO regional climate model. *Climate Dynamics*, *51*(11), 4525–4542. https://doi.org/10.1007/s00382-018-4085-7

Yang, Y., Chen, M., Zhao, X., Chen, D., Fan, S., Guo, J., & Ali, S. (2020). Impacts of aerosol–radiation interaction on meteorological forecasts over northern China by offline coupling of the WRF-Chem-simulated aerosol optical depth into WRF: A case study during a heavy pollution event. *Atmospheric Chemistry and Physics*, *20*(21), 12527–12547. https://doi.org/10.5194/acp-20-12527-2020

Yao, T., Piao, S., Shen, M., & Li, S., (2017). Chained impacts on modern environment of interaction between Westerlies and Indian Monsoon on Tibetan Plateau. *Bulletin of Chinese Academy of Sciences*, *32*(9), 976–984. https://bulletinofcas.researchcommons.org/journal/vol32/iss9/7/

Yu, B., Zhu, K., Xue, M., & Zhou, B. (2020). Using new neighborhood-based intensity-scale verification metrics to evaluate WRF precipitation forecasts at 4 and 12 km grid spacings. *Atmospheric Research*, *246*, 105117. https://doi.org/10.1016/j.atmosres.2020.105117

Yu, R., Li, J., Chen, H., & Yuan, W. (2014). Progress in studies of the precipitation diurnal variation over contiguous China. *Journal of Meteorological Research*, *28*(5), 877–902. https://doi.org/10.1007/s13351-014-3272-7

Zhang, C., Tang, Q., & Chen, D. (2017). Recent changes in the moisture source of precipitation over the Tibetan Plateau. *Journal of Climate*, *30*(5), 1807–1819. https://doi.org/10.1175/JCLI-D-15-0842.1

Zhang, X., Huang, A., Dai, Y., Li, W., Gu, C., Yuan, H., et al. (2022). Influences of 3D sub-grid terrain radiative effect on the performance of CoLM over Heihe River Basin, Tibetan plateau. *Journal of Advances in Modeling Earth Systems*, *14*(1), e2021MS002654. https://doi.org/10.1029/2021MS002654

Zhang, Y., Huang, A., & Zhu, X. (2006). Parameterization of the thermal impacts of sub-grid orography on numerical modeling of the surface energy budget over East Asia. *Theoretical and Applied Climatology*, *86*(1–4), 201–214. https://doi.org/10.1007/s00704-005-0209-1

Zhou, X., Yang, K., Beljaars, A., Li, H., Lin, C., Huang, B., & Wang, Y. (2019). Dynamical impact of parameterized turbulent orographic form drag on the simulation of winter precipitation over the Western Tibetan Plateau. *Climate Dynamics*, *53*(1), 707–720. https://doi.org/10.1007/s00382-019-04628-0

Zhu, K., Xue, M., Zhou, B., Zhao, K., Sun, Z., Fu, P., et al. (2018). Evaluation of real-time convection-permitting precipitation forecasts in China during the 2013–2014 summer season. *Journal of Geophysical Research: Atmospheres*, *123*(2), 1037–1064. https://doi.org/10.1002/2017JD027445

Zhu, K., Yu, B., Xue, M., Zhou, B., & Hu, X. M. (2021). Summer season precipitation biases in 4 km WRF forecasts over southern China: Diagnoses of the causes of biases. *Journal of Geophysical Research: Atmospheres*, *126*(23), e2021JD035530. https://doi.org/10.1029/2021JD035530